

activity criterion is hence the basis for a thermodynamically consistent new parameterization for  $J$  that improves and facilitates the simulation of homogeneous nucleation of ice clouds. Important applications range from issues like denitrification and future ozone depletion in the Arctic polar stratosphere to the aerosol indirect effect owing to homogeneously formed ice clouds in climate studies. The simplicity of the formulation makes it suitable not only for process studies but also for global-scale three-dimensional models. □

Received 3 December 1999; accepted 16 June 2000.

- Mishima, O. & Stanley, H. E. The relationship between liquid, supercooled and glassy water. *Nature* **396**, 329–335 (1998).
- Pruppacher, H. R. & Klett, J. D. *Microphysics Of Clouds And Precipitation* 79–80 & 205–215 (Kluwer, Dordrecht, 1997).
- Mishima, O. Relationship between melting and amorphization of ice. *Nature* **384**, 546–549 (1996).
- Kanno, H., Speedy, R. & Angell, C. A. Supercooling of water to  $-92^\circ\text{C}$  under pressure. *Science* **189**, 880–881 (1975).
- Rasmussen, D. H. Thermodynamics and nucleation phenomena - a set of experimental observations. *J. Cryst. Growth* **56**, 56–66 (1982).
- Kanno, H. & Angell, C. A. Homogeneous nucleation and glass formation in aqueous alkali halide solutions at high pressures. *J. Phys. Chem.* **81**, 2639–2643 (1977).
- Leberman, R. & Soper, A. K. Effect of high salt concentrations on water structure. *Nature* **378**, 364–366 (1995).
- Rasmussen, D. H. & MacKenzie, A. P. in *Water Structure at the Water Polymer Interface* (ed. Jellinek, H. G.) 126–145 (Plenum, New York, 1972).
- Weast, R. C. (ed.) *Handbook Of Chemistry And Physics* D139–D178 (Chemical Rubber Company, Cleveland, 1966).
- Baker, M. B. Cloud microphysics and climate. *Science* **276**, 1072–1078 (1997).
- Murphy, D. M., Thomson, D. S. & Mahoney, M. J. In situ measurements of organics, meteoritic material, mercury, and other elements in aerosols at 5 to 19 kilometers. *Science* **282**, 1664–1669 (1998).
- Johari, G. P., Fleissner, G., Hallbrucker, A. & Mayer, E. Thermodynamic continuity between glassy and normal water. *J. Phys. Chem.* **98**, 4719–4725 (1994).
- Gagnon, R. E., Kieffe, H., Clouter, M. J. & Whalley, E. Pressure dependence of the elastic constants of ice Ih to 2.8 kbar by Brillouin spectroscopy. *J. Chem. Phys.* **89**, 4522–4528 (1988).
- Dantl, G. in *Physics of Ice* (eds Riehl, N., Bullemer, B. & Engelhardt, H.) 223–230 (Plenum, New York, 1969).
- Hare, D. E. & Sorensen, C. M. The density of supercooled water. II. Bulk samples cooled to the homogeneous nucleation limit. *J. Chem. Phys.* **87**, 4840–4845 (1987).
- Mishima, O., Calvert, L. D. & Whalley, E. An apparently first-order transition between two amorphous phases of ice induced by pressure. *Nature* **314**, 76–78 (1985).
- Speedy, R. J., Debenedetti, P. G., Smith, R. S., Huang, C. & Kay, B. D. The evaporation rate, free energy, and entropy of amorphous water at 150K. *J. Chem. Phys.* **105**, 240–244 (1996).
- Koop, T., Ng, H. P., Molina, L. T. & Molina, M. J. A new optical technique to study aerosol phase transitions: the nucleation of ice from  $\text{H}_2\text{SO}_4$  aerosols. *J. Phys. Chem. A* **102**, 8924–8931 (1998).
- Chang, H. Y. A., Koop, T., Molina, L. T. & Molina, M. J. Phase transitions in emulsified  $\text{HNO}_3/\text{H}_2\text{O}$  and  $\text{HNO}_3/\text{H}_2\text{SO}_4/\text{H}_2\text{O}$  solutions. *J. Phys. Chem. A* **103**, 2673–2679 (1999).
- Koop, T., Bertram, A. K., Molina, L. T. & Molina, M. J. Phase transitions in aqueous  $\text{NH}_4\text{HSO}_4$  solutions. *J. Phys. Chem. A* **103**, 9042–9048 (1999).
- Bertram, A. K., Koop, T., Molina, L. T. & Molina, M. J. Ice formation in  $(\text{NH}_4)_2\text{SO}_4\text{-H}_2\text{O}$  particles. *J. Phys. Chem. A* **104**, 584–588 (2000).
- Angell, C. A., Sare, E. J., Donnella, J. & MacFarlane, D. R. Homogeneous nucleation and glass transition temperatures in solutions of Li salts in  $\text{D}_2\text{O}$  and  $\text{H}_2\text{O}$ . Doubly unstable glass regions. *J. Phys. Chem.* **85**, 1461–1464 (1981).
- Oguni, M. & Angell, C. A. Heat capacities of  $\text{H}_2\text{O}+\text{H}_2\text{O}_2$ , and  $\text{H}_2\text{O}+\text{N}_2\text{H}_4$  binary solutions: isolation of a singular component for  $c_p$  of supercooled water. *J. Chem. Phys.* **73**, 1948–1954 (1980).
- Schäfer, K. & Lax, E. (eds) *Landolt-Börnstein, Zahlenwerte und Funktionen* Part 2b (Springer, Berlin, 1962).
- Clegg, S. L., Brimblecombe, P. & Wexler, A. S. Thermodynamic model of the system  $\text{H}^+ - \text{NH}_4^+ - \text{SO}_4^{2-} - \text{NO}_3^- - \text{H}_2\text{O}$  at tropospheric temperatures. *J. Phys. Chem. A* **102**, 2137–2154 (1998).
- Krämer, B. *Laboruntersuchungen zum Gefrierprozess in polaren stratosphärischen Wolken* PhD thesis, Free University Berlin (1998).
- MacFarlane, D. R., Kadiyala, R. K. & Angell, C. A. Homogeneous nucleation and growth of ice from solutions. TTT curves, the nucleation rate, and the stable glass criterion. *J. Chem. Phys.* **79**, 3921–3927 (1983).
- Sassen, K. & Dodd, G. C. Homogeneous nucleation rate for highly supercooled cirrus cloud droplets. *J. Atmos. Sci.* **45**, 1357–1369 (1988).
- Heymsfield, A. J., Miloshevich, L. M., Twohy, C., Sachse, G. & Oltmans, S. Upper-tropospheric relative humidity observations and implications for cirrus ice nucleation. *Geophys. Res. Lett.* **25**, 1343–1346 (1998).
- Carlsaw, K. S. *et al.* Particle microphysics and chemistry in remotely observed mountain polar stratospheric clouds. *J. Geophys. Res.* **103**, 5785–5796 (1998).

## Acknowledgements

We are grateful to A. Bertram, C. Jeffery, G. Johari, O. Mishima, and H. Vortisch for helpful discussions and for providing us with original data sets. We also thank M. Canagaratna and J. Staehelin for helpful comments on manuscript drafts.

Correspondence and requests for materials should be addressed to T.K. (e-mail: koop@atmos.umnw.ethz.ch).

## Evidence from three-dimensional seismic reflectivity images for enhanced melt supply beneath mid-ocean -ridge discontinuities

G. M. Kent\*, S. C. Singh†‡§, A. J. Harding\*, M. C. Sinha‡§, J. A. Orcutt\*, P. J. Barton§, R. S. White§, S. Bazin\*‡, R. W. Hobbs†, C. H. Tong§ & J. W. Pye§

\* Cecil H. and Ida M. Green Institute of Geophysics and Planetary Physics, University of California, San Diego, La Jolla, California 92093, USA

† British Institutions Reflection Profiling Syndicate (BIRPS), § Department of Earth Sciences, Bullard Laboratories, University of Cambridge, Cambridge CB3 0EZ, UK

Quantifying the melt distribution and crustal structure across ridge-axis discontinuities is essential for understanding the relationship between magmatic, tectonic and petrologic segmentation of mid-ocean-ridge spreading centres. The geometry and continuity of magma bodies beneath features such as overlapping spreading centres can strongly influence the composition of erupted lavas<sup>1</sup> and may give insight into the underlying pattern of mantle flow. Here we present three-dimensional images of seismic reflectivity beneath a mid-ocean ridge to investigate the nature of melt distribution across a ridge-axis discontinuity. Reflectivity slices through the  $9^\circ 03' \text{ N}$  overlapping spreading centre on East Pacific Rise suggest that it has a robust magma supply, with melt bodies underlying both limbs and ponding of melt beneath large areas of the overlap basin. The geometry of melt distribution beneath this offset is inconsistent with large-scale, crustal redistribution of melt away from centres of upwelling<sup>2,3</sup>. The complex distribution of melt seems instead to be caused by a combination of vertical melt transport from the underlying mantle and subsequent focusing of melt beneath a magma freezing boundary in the mid-crust.

High-resolution swath mapping systems have provided dramatic images of mid-ocean plate boundaries, revealing a complex system that is segmented at a variety of scales<sup>2,4</sup>. For fast spreading rates, large-scale segmentation is defined by widely spaced transform faults, whose offsets are large enough to accommodate rigid slip. Ridge segments between transforms are further divided by a smaller ( $< 10 \text{ km}$ ) series of non-rigid plate boundaries, which can give the spreading centre a sinuous appearance. The largest non-transform offsets are recognized by their inward-curving limbs, which encircle an elongated depression<sup>5,6</sup>, and are usually sited at deeper portions of the ridge crest. Some investigators have attributed the morphological character of these “overlapping spreading centres” to a low magma supply<sup>2,5</sup>. These models of magmatic segmentation propose enhanced upwelling beneath the shallowest portions of the ridge crest, and, by inference, place large non-transform offsets along magmatically starved sections of the ridge, although there are models where along-axis flow is so efficient that magma supply is enhanced near ridge-axis discontinuities<sup>3</sup>. Petrologic sampling along mid-ocean ridges reveals a similar pattern of geochemical segmentation, suggesting an intimate connection between tectonic and magmatic segmentation of the ridge crest<sup>7</sup>. Other indicators of magmatic budget such as axial volume<sup>8</sup> and mantle Bouguer anomaly<sup>9</sup> tend to support the notion that the shallower, more

‡ Present addresses: Laboratoire de Sismologie, Institut de Physique du Globe de Paris, 75252 Paris Cedex 05, France (S.C.S., S.B.); School of Ocean and Earth Science, University of Southampton, Southampton SO14 3ZH, UK (M.C.S.).

inflated portions of the ridges are sites of enhanced magma injection from the mantle, which serve as the locus for redistribution of melt towards the distal ends of the segments. In contrast, seismic observations<sup>10–12</sup> across smaller discontinuities reveal a crustal magma chamber that is segmented at a scale of 10–15 km, providing evidence for only small-scale mixing of magma along the axis. Furthermore, the handful of reflection profiles<sup>13–15</sup> that cross overlapping spreading centres do not show a muted magma supply, but instead appear to show an abundance of melt near these features, suggesting a complex relationship between ridge-axis discontinuities and the underlying pattern of magmatic segmentation.

To differentiate between competing models of magmatic segmentation<sup>2,3,6</sup>, we conducted a three-dimensional seismic reflection survey across the 9° 03' N overlapping spreading centre, East Pacific Rise (Fig. 1). The ARAD (anatomy of a ridge-axis discontinuity) seismic experiment took place on board the RV *Maurice Ewing* in 1997. Thirty on-bottom hydrophones were also deployed to define the crustal velocity structure. Coincident three-dimensional images of seismic reflectivity and velocity represent the best approach for understanding the detailed structure across this ridge-axis discontinuity. The spatially dense layout of reflection profiles and on-bottom receivers was a necessity given the three-dimensional nature of the target. In this setting, widely spaced two-

dimensional seismic profiles would provide insufficient sampling of out-of-plane wave propagation, resulting in significant imaging errors. In addition, a complex, highly reflective sea floor can scatter out-of-plane energy onto a two-dimensional profile, producing coherent artefacts within the section, which can be especially acute in the mid-ocean-ridge environment. To overcome these difficulties, a series of 201 reflection profiles separated by 100 m were collected during the ARAD experiment to allow a full three-dimensional processing of the data. This scheme ensures that virtually all of the seismic wavefield will be accurately stacked and migrated, generating detailed images of crustal structure across this ridge-axis discontinuity.

Reflectivity slices through the three-dimensional volume reveal continuous melt sill events beneath both limbs of the overlapping spreading centre, with some melt-based reflections found underlying the northern overlap basin. The geometry of the melt sill underlying the western limb is relatively simple, showing a modest narrowing in width, but little or no depth variation along the ridge crest before dying out (Figs 2 and 3). In contrast, the melt sill beneath the propagating<sup>16</sup> eastern limb deepens significantly over its southernmost 6 km, plunging some 500 m in depth relative to the sea floor (Fig. 3). Unlike the melt sill beneath the western limb, which shows little morphological change with latitude, the melt sill

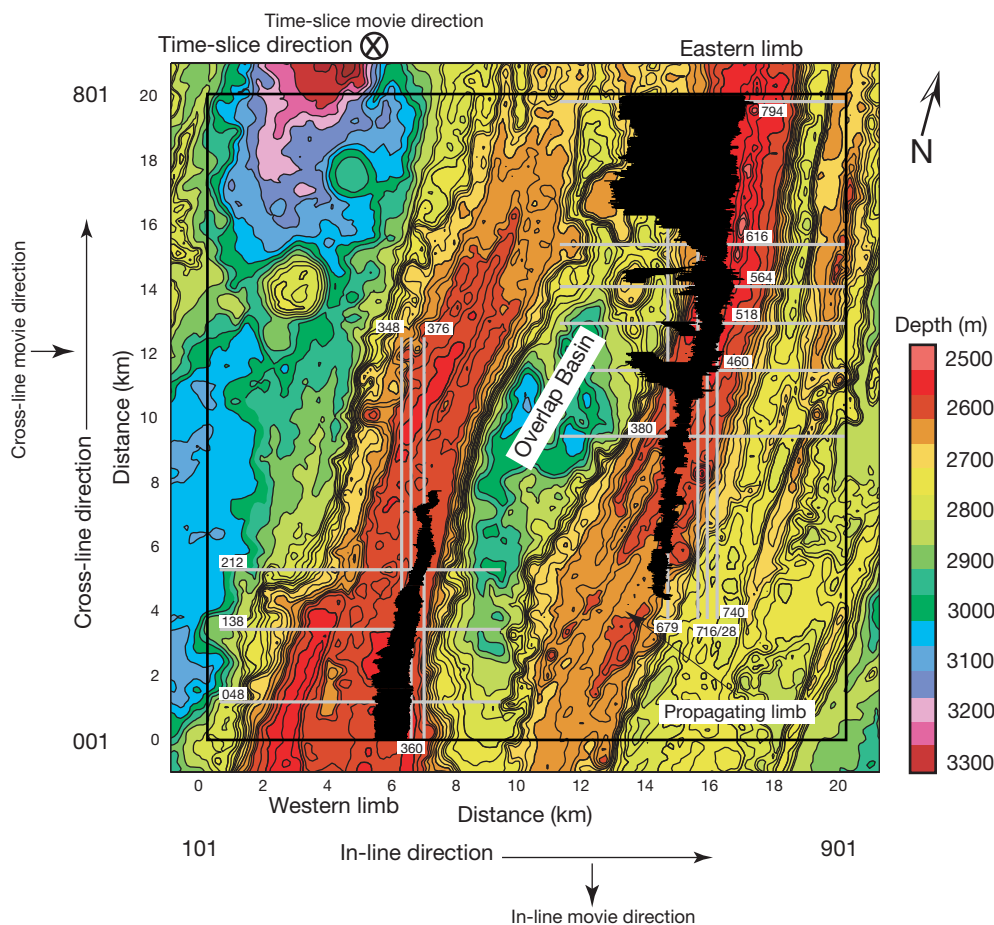


**Figure 1** Sea-floor bathymetry and nomenclature for the ARAD seismic experiment. Sea-floor depths were obtained from redundant (~30-fold) multibeam soundings obtained during the acquisition of the three-dimensional seismic volume. Bathymetry is contoured at 50-m intervals, with shallow regions of the discontinuity coloured red/orange to highlight the overlapping nature of the offset. Thin white lines show the location of seismic profiles presented in Figs 2 and 3. The areal extent of crustal magma chambers are shown as black in-fill overlying sea-floor bathymetry. Seismic volume coordinates are also

indicated. The in-line direction corresponds to the sailing direction during data acquisition, while the cross-line direction is perpendicular to the sail-line azimuth. Individual in- and cross-line slices are separated by 25 m. In-line slices range from 1 to 801, while cross-line slices range from 101 to 901. Time-slices are oriented orthogonal to the plane defined by in- and cross-line directions, and are separated by 4-ms increments. Forward-play directions of Supplementary Information movie frames are also indicated.

geometry beneath the eastern limb is very complex. To the north, the melt horizon is displaced westward of the ridge-axis toward the overlap basin, and is some 4 km in width (Fig. 2, slice 794). The melt sill in this region also appears to be offset by a constant travel-time delay from the layer 2A reflection; if the layer 2A reflection represents the extrusive-dyke contact<sup>17–20</sup>, then this geometry suggests that the melt sill may follow a permeable pathway just below the base of the sheeted-dyke complex. Ultimately, a ridge-centred melt lens<sup>21</sup> becomes dominant along the southern reaches of the propagating ridge tip, but is occasionally supplied by discrete conduits of melt, which originate beneath the central overlap basin. This observation suggests that melt ascending beneath the overlap basin is an important source for lavas erupted along the propagating limb. It should also be noted that although the plunging melt sill beneath the propagating tip is continuous, its width remains remarkably narrow, typically less than 500 m over its last 3–4 km of existence.

Three-dimensional images of seismic reflectivity across this large non-transform offset do not show a continuous melt sill underlying the entire basin, which presumably rules out mixing of melt between the western and eastern limbs, although these ridge-crest magma reservoirs may have a common source beneath the overlap basin. The reflection images are further supported by on-bottom-recorded, wide-angle refracted arrivals, which clearly show a sig-

nificant low-velocity zone underlying the entire basin<sup>22</sup>. The near-axis permeability structure of the mid- to upper-crust is probably controlled by the base of the sheeted-dyke complex, plus any small amounts of isotropic gabbros which have solidified<sup>23</sup>. Thus, melt ascending vertically beneath the basin floor will probably be focused along this permeability front, which may explain both the extended melt horizons found dipping upwards toward the neovolcanic zone along the eastern limb, and why these features, to first-order, are found at a constant travel-time beneath the presumed extrusive-dyke contact<sup>15</sup>. Moreover, regardless of magma budget, the likelihood of maintaining a continuous melt sill beneath the basin is low, as melt would have to coalesce beneath a permeability front, which is synclinal in form. Instead, it is more likely that the buoyant melt would migrate up-dip towards the neovolcanic zones beneath each limb, where there is closure within the permeability structure; this capture mechanism is analogous to the migration of buoyant gas and oil towards anticlinal structures where these fluids are then trapped against an impermeable barrier. Ultimately, the thermal state of the ridge crest<sup>24</sup> is controlled by the permeability structure, which sets the sheeted-dyke thickness, and the growth rate of isotropic gabbros, which together form a seal that focuses melt towards delivery along the neovolcanic zone.

A clear understanding of the three-dimensional structure beneath a large ridge-axis discontinuity provides new insights into the

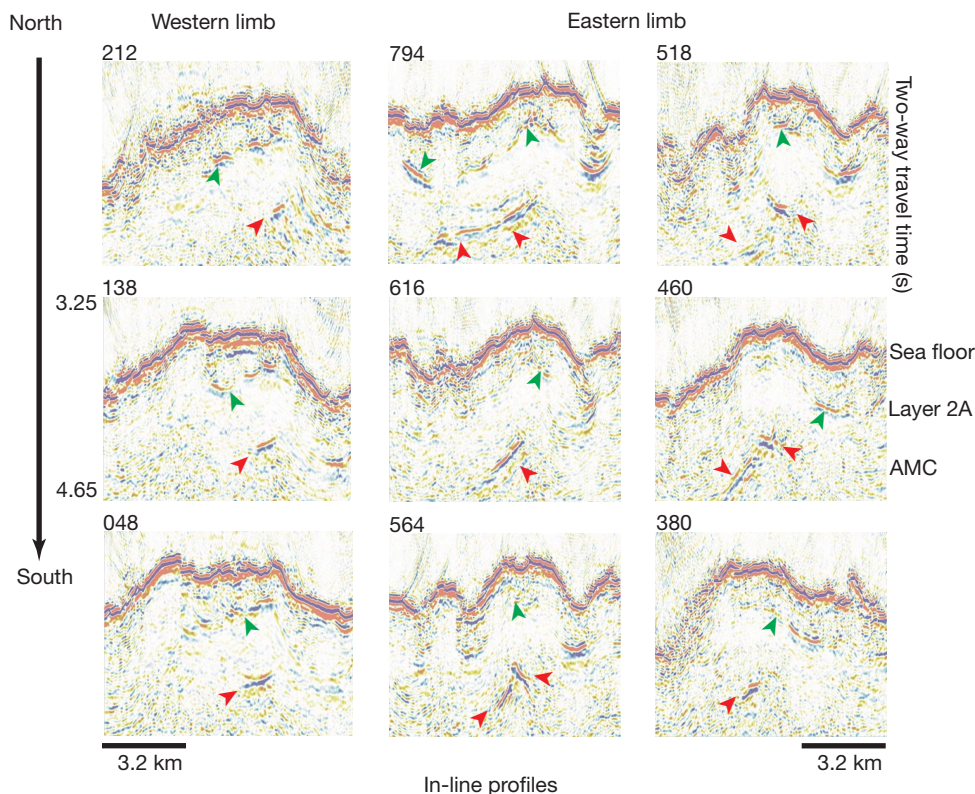


**Figure 2** In-line seismic reflectivity slices through the western and eastern limbs of the 9° 03' N overlapping spreading centre. Axial magma chambers and seismic layer 2A reflectors are highlighted with red and green arrows, respectively. The three-dimensional melt sill structure beneath the western limb is relatively simple, showing a gradual decrease in melt sill width from 1,100 m (slice 048) beneath an inflated axial ridge, to less than 375 m (slice 212) some 4 km northwards, just before the melt sill event disappears (see Fig. A1 in Supplementary Information). In contrast to the western limb, the melt sill structure beneath the eastern limb is very complex. To the north, the eastern limb is dominated by a westward-displaced melt sill (slice 794), which underlies the overlap basin. This feature shows little change for 4 km along-strike, then its width quickly tapers down to <1,500 m (slice 616). Southwards, a second melt sill event is seen dipping toward the east, producing a 'tent-shaped' magma chamber morphology (slice 564).

Next, a ridge-centred sill is observed (slice 518), with an intermittent, secondary melt sill extending from the central overlap basin, upwards toward the primary sill (slice 460). These secondary events demonstrate that the ridge-centred melt sill beneath the eastern limb is fed, in part, from magma upwelling beneath the overlap basin. The ridge-centred melt sill continues to deepen (slice 380) towards the propagating ridge tip; despite its narrow width (< 500 m), this event is nearly continuous along the axis, until it finally dies out near the propagating tip. Time-slice seismic reflectivity maps through the western and eastern limbs are available; see Fig. A1 in Supplementary Information. Slice-by-slice cross-dip views of the melt sill beneath both limbs are available as Supplementary Information movies "In-line Western Limb" and "In-line Eastern Limb". AMC, axial magma chambers.

process and coupling of magmatic, tectonic and petrologic segmentation of the ridge crest. The three-dimensional nature of melt distribution across this offset (Fig. 4a) appears to be inconsistent with large-scale, crustal redistribution of melt away from centres of upwelling some 50–100 km distant<sup>23</sup>; there are two reasons why this is the case. First, the melt sill along the propagating limb has a tortuous morphology with contributions from magma sources beneath the overlap basin. This geometry is hard to explain by simple along-axis flow away from a distant centre of upwelling, as such flow would require moving buoyant material to deeper levels within the crust, with a significant off-axis component of deflection toward the overlap basin. Second, it is interesting to note that the deepening of the axial magma chamber away from the inferred centre of upwelling is approximately 250 m over the first 90 km (refs 15, 25), but then plunges twice that amount over the last 6 km. The increased gradient over the last 6 km is most probably related to variations in the rheology and thermal structure of the overlying

upper crust at the propagating southern tip of the eastern limb, although this depth increase may be related to the injection of melt into the propagator<sup>26</sup>, and the associated hydraulic head loss within the reservoir. The latter scheme is more plausible if a sustaining low-velocity zone is either muted or non-existent beneath the southern tip. Interestingly, the magma reservoir makes several small (200 m)

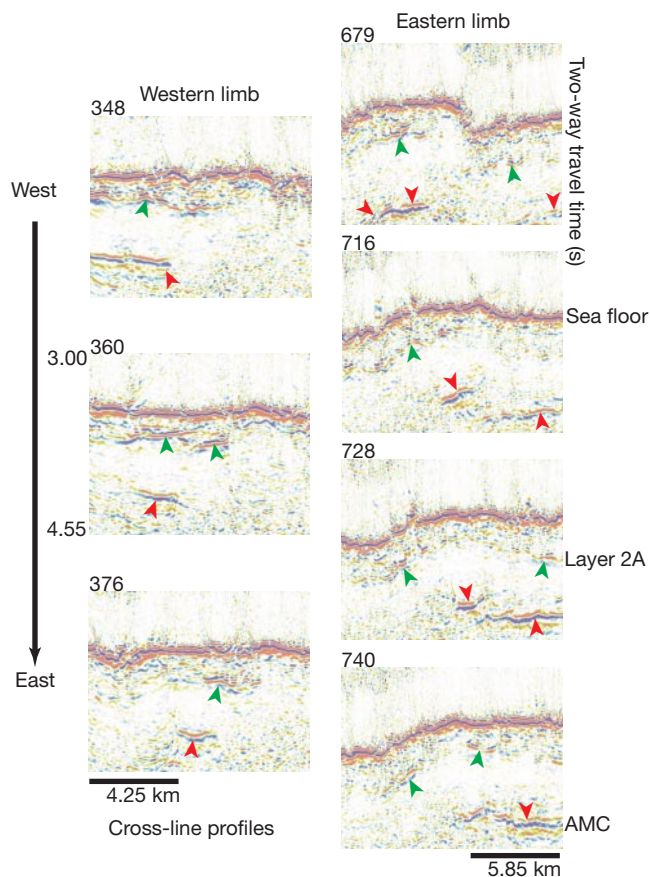


**Figure 3** Cross-line seismic reflectivity slices through the western and eastern limbs of the 9° 03' N overlapping spreading centre. Axial magma chambers and seismic layer 2A reflectors are highlighted with red and green arrows, respectively. Three cross-line slices illustrate the simpler axial geometry of the melt lens beneath the western limb, although changes in layer 2A thickness might control (assuming constant-thickness layer 2B) the exact location of the melt sill (slice 360) beneath the ridge crest. Four in-line slices through the eastern limb (and overlap basin) show an abrupt decrease in magma chamber depth (slices 716 and 728) moving southwards along the propagating ridge tip, where melt sill morphology changes from a westward-displaced event into a ridge-centred system. Further along the propagating tip (southwards), the melt horizon shows a significant increase in depth relative to either sea-floor or layer 2A events (roughly 500 m depth over 6 km of ridge length), indicative of rapid changes in thermal, rheology and permeability structure beneath the propagating tip of this limb. Supplementary Information movies “Cross-line Western Limb” and “Cross-line Eastern Limb” allow a slice-by-slice along-strike view of the melt sill beneath both limbs.

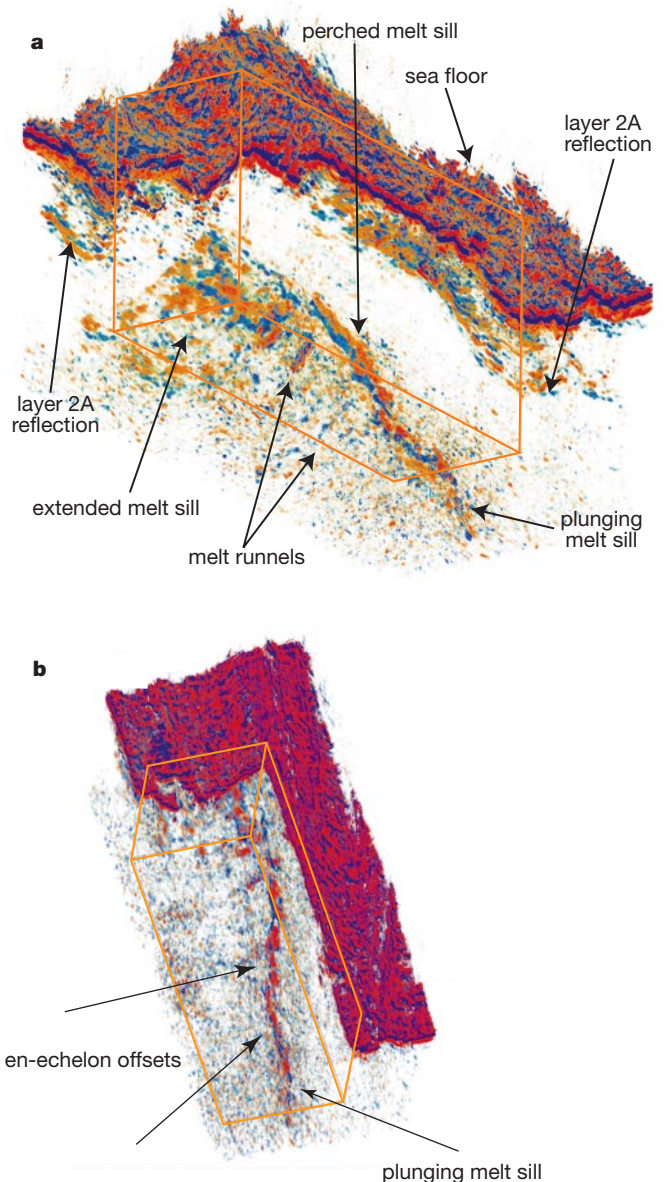


**Figure 4** Three-dimensional visualization of magma chamber structure. **a**, Three-dimensional rendering of seismic reflectivity beneath the eastern limb of the 9° 03' N overlapping spreading centre, East Pacific Rise. A corner-cut (orange frame) has been made to allow viewing of the magma chamber reservoir (orange and blue-green hues), through the sea-floor and layer 2A reflections (red and blue hues). This oblique perspective of the magma chamber structure highlights the abundance of melt beneath both the northern overlap basin and the propagating limb of this large ridge-axis discontinuity. The complex melt sill morphology underlying the eastern limb is inconsistent with large-scale, along-axis crustal flow or migration of magma from a distant centre of upwelling. **b**, A close-up view of fine-scale magma chamber structure beneath the propagating eastern limb. Note the en-echelon behaviour of the plunging melt sill, which suggests melt migration within mid-crustal fractures or cracks. Relevant movies are available as Supplementary Information; ‘ARAD\_Infill’ and ‘ARAD\_Spin’ for **a**, ‘ARAD\_Tilt’ for **b**.

right-lateral steps (Fig. 4b) within the zone of deepening, which is suggestive of melt injection through en-echelon, mid-crustal cracks or fractures. This mode of rift-tip injection might also explain the asymmetry of melt between the two limbs.

Lavas erupted near the propagating tip of this offset<sup>27</sup> were found to have high concentrations of titanium and iron oxides, which led investigators to suggest that these Fe-Ti basalts were derived from isolated magma bodies within the rift-tip<sup>1</sup>. The largest magnetic anomaly in this region<sup>27</sup>, delimiting the inferred zone of Fe-Ti basalts, coincides with the downward-plunging section of the magma chamber. The current melt sill morphology rules out an isolated melt body, although the en-echelon structure of the plunging melt sill would probably reduce any along-axis mixing of magma. Thus, the resultant geochemistry may better reflect the thermal environment within the propagating limb, or possibly a short-wavelength, along-axis fractionation trend<sup>28</sup>.

Estimates of crustal<sup>29</sup> and extrusive<sup>17</sup> thickness surrounding the overlap region are significantly greater than observed near 9° 50' N, which is the inferred focus of magma supply for this segment<sup>2,3</sup>. If the current mode of melt emplacement along this ridge segment has remained more or less constant on a timescale of 10–100 kyr, or remained stationary with respect to the propagating offset, then it is unlikely that any large-scale crustal redistribution of melt is responsible for thickened crust throughout this region, although sub-crustal migration and focusing of melt cannot be ruled out. An alternative, simpler explanation requires only small-scale (a few tens of kilometres) redistribution of melt along the ridge crest<sup>10–12</sup>, which could be further modified through focusing along permeable pathways within the middle to upper crust. □

## Methods

### Navigation and binning

The hydrophone array used during the ARAD experiment was a 3,100-m-long, 124-channel Digicon DMS-2000 streamer. Shipboard navigation was achieved by an Inmarsat-based differential GPS system with an accuracy of a few metres. Streamer positioning was reconstructed using bearing measurements (with an accuracy of a few tenths of a degree) from 12 Digicon compass birds placed at 250 m intervals along the streamer. Streamer positioning was checked against GPS fixes from the streamer tailbuoy, which confirmed our solution with along- and cross-track errors no greater than 15 and 30 m, respectively. Individual shot records from a 10-gun (50-litre) source array were spaced 38 m apart, and were binned according to common-midpoint location between source and receiver. To achieve even offset coverage, a flexible binning strategy was adopted whereby individual bins (25 m × 100 m) were overlapped by 50% in the cross-line direction. Bin extension lessens the effect of uneven coverage at a given source–receiver range, which is rooted in the variability of streamer shape throughout the experiment. Eight additional profiles were collected to fill in the most serious gaps in data coverage.

### Stacking and migration

Three-dimensional images of seismic reflectivity were obtained through the analysis of some 120,000 shot records. The > 13 million binned traces were spike-edited, filtered, corrected for spherical divergence and normal moveout, and stacked. The resultant 20 km × 20 km stacked volume was first in-line migrated at the water velocity to collapse steeply dipping diffractions originating at the sea floor, followed by cross-line interpolation onto 25 m × 25 m cells. The interpolated data volume was then cross-line migrated at the water velocity to collapse any remaining sea-floor-diffracted energy. Lastly, the entire data volume was finite-difference time-migrated (two-pass) using residual velocities<sup>30</sup> to produce a geometrically correct version of the sea floor and underlying features such as melt sills, extrusive layer-dyke contacts and Moho. The interpretations presented here are based on the migrated three-dimensional time-image, with conversions to depth, where given, based on a composite velocity function<sup>17</sup> that accounts for lateral variations in layer 2A thickness. The mapping of events into depth based on this scheme assumes that deepening of the 2A interface in travel time can be, to first order, accounted for through an increase in thickness and velocity of the surficial layer, along with a systematic relaxation of the velocity gradient at the base of layer 2A<sup>17</sup>.

Received 29 November 1999; accepted 9 June 2000.

- Sinton, J. M., Wilson, D. S., Christie, D. M., Hey, R. N. & Delaney, J. R. Petrologic consequences of rift propagation on oceanic spreading ridges. *Earth Planet. Sci. Lett.* **62**, 193–207 (1983).
- Macdonald, K. C. *et al.* A new view of the mid-ocean ridge from the behaviour of the ridge-axis discontinuities. *Nature* **335**, 217–225 (1988).
- Wang, X., Cochran, J. R. & Barth, G. Gravity anomalies, crustal thickness and the pattern of mantle flow at the fast spreading East Pacific Rise, 9°N–10°N: Evidence for three-dimensional upwelling. *J. Geophys. Res.* **101**, 17927–17940 (1996).

- Lonsdale, P. Segmentation of the Pacific-Nazca spreading center, 1°N–20°S. *J. Geophys. Res.* **94**, 12197–12225 (1989).
- Macdonald, K. C. & Fox, P. J. Overlapping spreading centres: new accretion geometry on the East Pacific Rise. *Nature* **302**, 55–58 (1983).
- Lonsdale, P. Overlapping rift zones at the 5.5°S offset of the East Pacific Rise. *J. Geophys. Res.* **88**, 9393–9406 (1983).
- Langmuir, C. H., Bender, J. F. & Batiza, R. Petrologic and tectonic segmentation of the East Pacific Rise, 5°30'–14°30'N. *Nature* **322**, 422–429 (1986).
- Scheirer, D. S. & Macdonald, K. C. Variation in cross-sectional area of the axial ridge along the East Pacific Rise: Evidence for the magmatic budget of a fast spreading center. *J. Geophys. Res.* **98**, 7871–7886 (1993).
- Magde, L. S., Detrick, R. S. & TERA Group. Crustal and upper mantle contribution to the axial gravity anomaly at the southern East Pacific Rise. *J. Geophys. Res.* **100**, 3747–3766 (1995).
- Toomey, D. R., Purdy, G. M., Solomon, S. C. & Wilcock, W. S. D. The three-dimensional seismic velocity structure of the East Pacific Rise near latitude 9°30'N. *Nature* **347**, 639–645 (1990).
- Singh, S. C., Kent, G. M., Collier, J. S., Harding, A. J. & Orcutt, J. A. Melt to mush variations in crustal magma properties along the ridge crest at the southern East Pacific Rise. *Nature* **394**, 874–878 (1998).
- Dunn, R. A. & Toomey, D. R. Seismological evidence for three-dimensional melt migration beneath the East Pacific Rise. *Nature* **388**, 259–262 (1992).
- Mutter, J. C. *et al.* Magma distribution across ridge axis discontinuities on the East Pacific Rise (8°40' to 9°50' North) from multichannel seismic images. *Nature* **336**, 156–158 (1988).
- Collier, J. S. & Sinha, M. C. Seismic images of a magma chamber beneath the Lau Basin back-arc spreading centre. *Nature* **346**, 646–648 (1990).
- Kent, G. M., Harding, A. J. & Orcutt, J. A. Distribution of magma beneath the East Pacific Rise near the 9°03'N overlapping spreading center from forward modeling of common depth point data. *J. Geophys. Res.* **98**, 13971–13996 (1993).
- Carbotte, S. & Macdonald, K. C. East Pacific Rise 8°–10°30'N: Evolution of ridge segments and discontinuities from SeaMARC II and three-dimensional magnetic studies. *J. Geophys. Res.* **97**, 6959–6982 (1992).
- Harding, A. J., Kent, G. M. & Orcutt, J. A. A multichannel seismic investigation of the upper crustal structure at 9°N on the East Pacific Rise: Implications for crustal accretion. *J. Geophys. Res.* **98**, 13925–13944 (1993).
- Carbotte, S., Mutter, J. C. & Wu, L. Contribution of volcanism and tectonism to axial and flank morphology of the southern East Pacific Rise, 17°10'–17°40', from a study of layer 2A geometry. *J. Geophys. Res.* **102**, 10165–10184 (1997).
- Christeson, G. L., Kent, G. M., Purdy, G. M. & Detrick, R. S. Extrusive thickness variability at the East Pacific Rise, 9°–10°N: Constraints from seismic techniques. *J. Geophys. Res.* **101**, 2859–2873 (1996).
- Hooff, E. E. E., Schouten, H. & Detrick, R. S. Constraining crustal emplacement processes from the variation of seismic layer 2A thickness at the East Pacific Rise. *Earth Planet. Sci. Lett.* **142**, 289–309 (1996).
- Kent, G. M., Harding, A. J. & Orcutt, J. A. Evidence for a smaller magma chamber beneath the East Pacific Rise at 9°30'N. *Nature* **344**, 650–653 (1990).
- Bazin, S. *Three-dimensional Crustal Structure of East Pacific Rise Discontinuities from Tomographic Inversions*. Thesis, Univ. California, San Diego (2000).
- Singh, S. C., Collier, J. S., Harding, A. J., Kent, G. M. & Orcutt, J. A. Seismic evidence for a hydrothermal layer above the solid roof of the axial magma chamber at the southern East Pacific Rise. *Geology* **27**, 219–222 (1999).
- Phipps Morgan, J. & Chen, Y. J. The genesis of oceanic crust: Magma injection, hydrothermal circulation, and crustal flow. *J. Geophys. Res.* **98**, 6283–6297 (1993).
- Detrick, R. S. *et al.* Multichannel imaging of the axial magma chamber along the East Pacific Rise between 9°N and 13°N. *Nature* **326**, 35–41 (1987).
- Phipps Morgan, J. & Parmentier, E. M. Causes and rate-limiting mechanisms of ridge propagation: a fracture mechanics model. *J. Geophys. Res.* **90**, 8603–8612 (1985).
- Sempéré, J.-C., Macdonald, K. C. & Miller, S. P. Overlapping spreading centres: 3-D inversion of the magnetic field at 9°03'N on the East Pacific Rise. *Geophys. J. R. Astron. Soc.* **79**, 799–811 (1984).
- Batiza, R. & Mutter, J. C. Variability in oceanic crustal thickness and structure: Multichannel seismic reflection results from the northern East Pacific Rise. *J. Geophys. Res.* **101**, 17951–17975 (1996).
- Barth, G. A. & Mutter, J. C. Variability in oceanic crustal thickness and structure: Multichannel seismic reflection results from the northern East Pacific Rise. *J. Geophys. Res.* **101**, 17951–17975 (1996).
- Yilmaz, O. *Seismic Data Processing* (Society of Exploration Geophysicists, Tulsa, 1987).

Supplementary information is available on Nature's World-Wide Web site (<http://www.nature.com>) or in CD-ROM format from the author.

### Acknowledgements

We thank the officers and crew of the RV *Maurice Ewing* for around-the-clock help during the 47-day-long cruise; H. Avendonk, D. Boschi, A. Cherrett, A. Greer, P. Henkart, C. Hollinshead, S. Husenoeder, T. Owen and P. Zimmer for assistance with instrumentation and watch-standing duties during the experiment; and R. Detrick and D. Toomey for comments that significantly improved this Letter. Data-processing software was provided by Paradigm Geophysical, Houston, Texas. Focus 3-D was used for the three-dimensional binning, stacking and migration of the multichannel seismic data. Data presentation of the three-dimensional volume was facilitated through visualization modules within Focus 3-D and VoxelGeo. The ARAD seismic experiment is an international collaborative project between investigators at the Scripps Institution of Oceanography and the University of Cambridge, with financial support from the RIDGE program/National Science Foundation (USA), British Institutions Reflection Profiling Syndicate (BIRPS), and the Natural Environment Research Council (UK). Additional matching funds for computer visualization and data storage were provided by the Scripps Institution of Oceanography and the Cecil H. and Ida M. Green Foundation for Earth Sciences.

Correspondence and requests for materials should be addressed to G.M.K. (e-mail: gkent@ucsd.edu).